SENSITIVITY ANALYSIS OF TUSCALOOSA SANDSTONES TO CO_2 SATURATION, CRANDIELD FIELD, CRANFIELD, MS.

Russell Carter

Department of Geological Sciences
The University of Texas at Austin

ABSTRACT

Advances are continually being made in the field of seismic reservoir characterization, but many problems exist in characterizing the lateral extent and volume of injected CO_2 in subsurface formations using well log and seismic data. In this study I use rock physics modeling, fluid substitution, AVA analysis, and statistical classification to analyze and model well log data. These tools are used to better understand how to effectively characterize and monitor CO_2 injected into a brine reservoir. Rock physics modeling was initially completed to obtain reservoir parameters, which were then used to generate synthetic velocity and density logs for different fluid mixtures. The synthetic logs were used in a Monte Carlo AVA simulation and statistical rock physics analysis. The rock physics modeling showed that the reservoir was a stiff cemented sandstone. The AVA analysis indicated that the cemented sandstone was sufficiently stiff that the fluid component was not easily discernable. Additionally, the contrast between the shale seal and the reservoir was sufficiently large that AVA analysis did not show useful difference among different CO_2 concentrations at this study area. However, when using the statistical rock physics to differentiate between CO_2 and brine, Vp/Vs was an important parameter to use to maximize percentages of correctly mapping modeled data to its respective fluid class. This is important because it illustrates the sensitivity and uncertainty of using elastic properties to characterize CO_2 saturation at this site.

INTRODUCTION

Quantitative seismic interpretation techniques have been used with great success in locating and characterizing hydrocarbon reservoirs (Bosch et al., 2009; Russell et al., 2003; Mukerji et al., 2001; and Avseth et al., 2011). These techniques are well developed, and in many cases they are quite accurate in relating seismic velocity to fluid saturation and other reservoir properties of interest. This study aims to use and adapt these techniques for use in a reservoir containing injected CO_2. Injected CO_2 has very different physical properties than hydrocarbons when contained within reservoirs. Injection of CO_2 is increasingly being used as a means of enhanced oil recovery (EOR), and there is a steady push towards injecting CO_2 as a means of permanent sequestration. Because of these applications, it is important to understand how injected CO_2 affects the elastic parameters of reservoirs. Conventional fluid substitution work focused primarily on modeling elastic properties and seismic data with different fluid-saturation scenarios to help distinguish between brine and hydrocarbon reservoirs (Das and Batzle, 2008; Artola and Alvarado, 2006). Only recently has interest grown to model the effects of CO_2 on the elastic properties of the reservoir.

Recent studies completed on CO_2 injection and monitoring have covered a wide range of topics. The feasibility of time-lapse seismic monitoring of CO_2 saturation has been looked at by Lumley (2010) who studied the fluid properties of CO_2 as a function of temperature, pressure and saturation. The same study also outlined the challenges of time-lapse monitoring of CO_2, including repeatability, CO_2-rock interactions, in situ CO_2 properties, pressure changes, and non-uniqueness. Time-lapse applications have been completed by Ghaderi and Landro (2009) who examined amplitude and time shifts to estimate thickness and velocity changes in the Sleipner field. Processing techniques for using time-lapse vertical seismic profiles (VSPs) as a means of monitoring CO_2 was completed by Cheng at al. (2010). Their findings were that VSP data could be used for time-lapse monitoring of CO_2 injection, provided that the processing between vintages of VSPs was performed to equalize first-break time alignment, frequency spectra, and gain levels. Work done to image CO_2 plumes using simulated crosswell data has been done by Morency et al. (2011) using finite-frequency sensitivity kernels. They compared the results of using compressional versus elastic wave modeling. Including shear wave data in their simulations improved the resolution of their results. A quantitative approach to seismic monitoring of CO_2 was taken by Chadwick et al. (2010). They looked at multiple vintages of data from the Sleipner field and applied a prestack stratigraphic inversion algorithm and compared it to poststack inversion methods. Prestack inversion characterized better thin intra-reservoir mudstone and sand layers compared to using poststack inverstion.

This study differs from previous studies as it combines rock physics modeling, fluid substitution and statistical analysis to differentiate between brine and CO_2 saturated zones in the reservoir. Data for this work comes from the Cranfield reservoir located in Cranfield, MS. The data set includes well-log data from both injection and monitoring wells, 3-D time-lapse surface seismic data, and time-lapse VSP data. This study used Gassmann (1951) fluid substitution to model a shale-sandstone interface with varying mixtures of CO_2 and brine in the underlying sand interval. A shale-sandstone interface was chosen to represent the interface between the top of the reservoir and the overlying shale layer. Due to buoyant rising of CO_2 it is anticipated that injected CO_2 will rise and accumulate along this interface. From the modeled data, amplitude versus angle (AVA) analysis was completed to see the effects of increasing levels of CO_2 on the angle-dependent reflectivity. AVA signatures have proven useful in identifying natural gas and have been organized into different classes (Rutherford and Williams, 1989; Castagna et al., 1998; and Simm et al., 2000). Reflection coefficients from the AVA analysis were plotted against modeled data from the fluid substitution analysis for use in a statistical classification scheme. The classification scheme compared modeled data to multiple probability density functions (PDFs) to determine which PDF had the highest probability at the data location.

DATASET

The Cranfield study area consists of a sandstone reservoir of the Lower Tuscaloosa Formation, which is dated as Upper Cretaceous. The reservoir has porosity of about 20% and permeabilites in the range of 0.1–1000 millidarcies (Lu, et al., 2012). Regionally the reservoir and seals are part of a sequence of sands and shales that are found in the Late Cretaceous Tuscaloosa Groups. A salt body underlies the entire complex, whose buoyancy is forcing a local

anticline. A large regional seal of marine shale and mudstone exists in the Middle Tuscaloosa Formation (Lu et al., 2012).

The Cranfield Field reservoir was discovered in 1943 and subsequently abandoned in 1966. The site was recently selected as a location for EOR using CO_2 injection (Lu et al., 2012) due to regional infrastructure, regionally available CO_2 and the high potential of economical, enhanced oil and gas production. The Gulf Coast Carbon Center of the Bureau of Economic Geology at the University of Texas at Austin is working in conjunction with both the Southeast Regional Carbon Sequestration Partnership and the field operator on the project (Lu et al., 2012). Over the entire field, the operator has injected a total of 2.5 million tons of CO_2 since the start of injection. Data for this project comes from the 1 km^2 Detail Area Study (DAS), outlined in red in Figure 1. The DAS consists of 1 injection well and two down dip monitoring wells (CFU 31#F1, 2, and 3, respectively) injection rates at CFU 31#F1 (F-1) ranged from 200–500 tons per day during injection. Data used for this project came from the observation well, CFU 31#F2 (F-2).

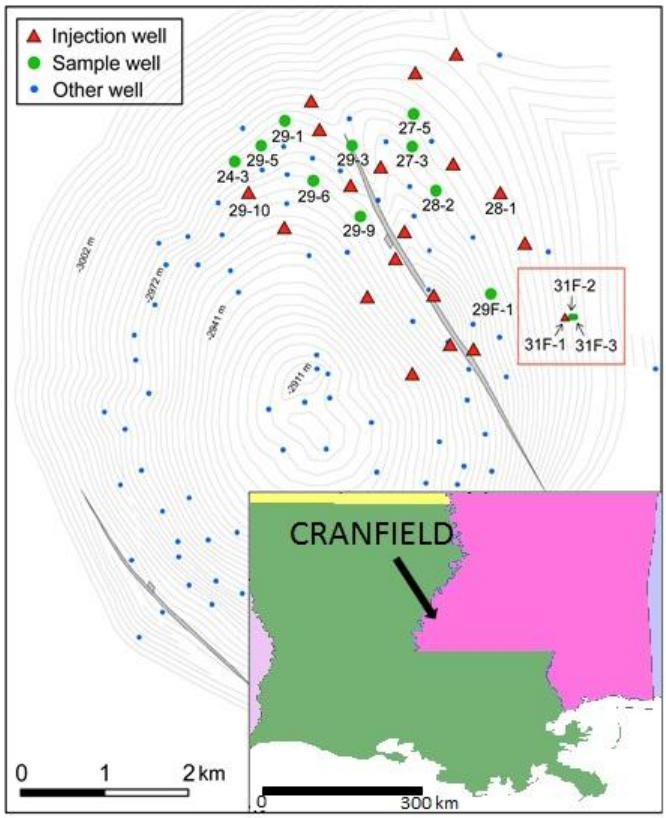

Figure 1. The entire Cranfield site. Data for this project came from the DAS (red box). The DAS contains one injection well, 31F-1 (F-1), and two monitoring wells, 31F-2 (F-2) and 31F-3 (F-3). Modified from Lu et al. (2012).

Figure 2 shows the Vp, Vs, and gamma ray logs in the reservoir interval for well F-2. Data from the well logs show two distinct layers. The blue line shows the entire reservoir zone, the red overlies the upper reservoir zone from about 10445 to 10480 feet and the green overlay indicates the lower reservoir zone at approximately 10485 to 10500 feet. The increase in the gamma ray count at about 10485 ft indicates that a shale layer divides the upper and lower reservoir zones.

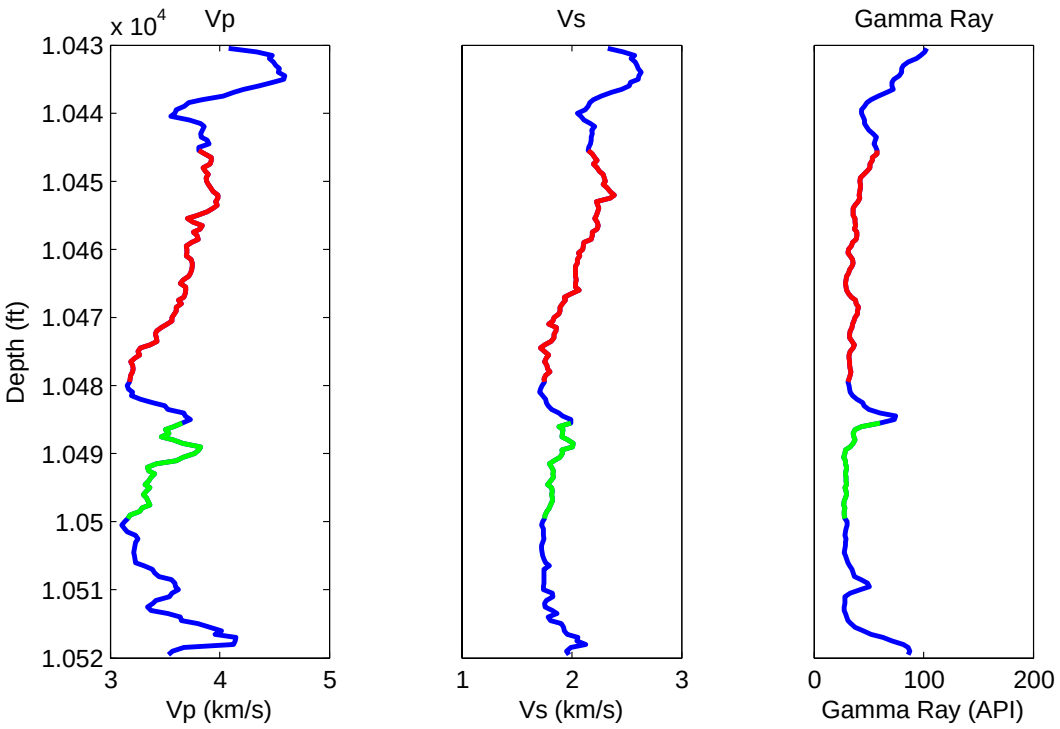

Figure 2. Well F-2. The red line shows the shallower reservoir zone, which extends from about 10445 to 10480 ft and the green line shows the deeper reservoir zero, which extends from about 10485 to 10500. The shale layer that divides the two reservoir zones is apparent from the increase in the gamma ray count between 10480 and 10490 ft.

THEORY AND METHODS

This study was a multi-step process that integrated rock physics modeling, fluid substitution, AVA and statistical classification. Rock physics modeling linked reservoir properties to elastic parameters for use in the fluid substitution and AVA phases of this project. Statistical classification was then run on the results from the fluid substitution and the AVA. The results from the statistical classification indicated which combinations of elastic properties provided the best discrimination of different CO_2-brine mixtures.

Rock Physics Modeling

Contact theory models are based on the idea that by changing the number of grain contacts and the stiffness of these contacts the overall stiffness of the rock will be changed (Dvorkin et al., 1991, and Dvorkin et al., 1994). The contact cement model, used in this study, is based on contact theory with the addition of cement at grain contacts. In the model cement can be deposited in one of two ways (Figure 3). The first approach is to deposit cement concentrically and evenly around each grain. This coats the grains and subsequently decreases porosity. The second method of cement deposition places cement only at the grain boundaries. For purposes of this model, the first technique of cement deposition was used.

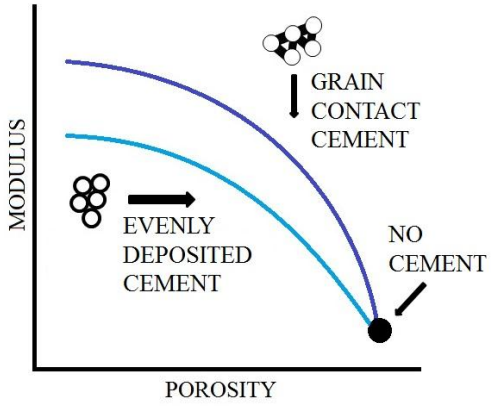

Figure 3. A schematic of the contact cement model. Cement can be deposited concentrically around the grain following the lower path on the graph or only at grain contacts, following the upper line on the graph. As cementation increases, porosity decreases, and the elastic moduli increase.

Petrography studies on core samples from the F-2 well indicate that mineral composition of the reservoir consisted of 60-80% quartz, 10-20% clay, and 10-20% feldspar, with the remainder composed of small percentages of muscovite, calcite, and other minerals (Kordi et al., 2010). These compositions were used to calibrate the Hashin-Shtrikman (1963) bounds. In turn these bounds were used to provide rock-frame moduli at different porosities for use in the contact cement model (Dvorkin and Nur, 1996). Models corresponding to this method explained the trend in the data from the shallower portion of the reservoir (Figure 4). For the deeper portion of the reservoir a modified Hashin-Shtrikman lower bound was used (Figure 5) (Avseth et al., 2005). The modified Hashin-Shtrikman lower bound can be implemented to represent sorting trends in the data. This lower bound shows that the grains in the shallower part of the modeled interval are relatively well sorted compared to the grains in the deeper portion of the modeled interval. This model provides an interpretation for the deeper reservoir interval of a grain pack with a mixture of both coarse and fine grains, which causes a lower porosity than the well sorted grains of the shallower portion. The contact cement model and the modified Hashin-Shtrikman lower bound provide accurate and predictive starting rock models for this study.

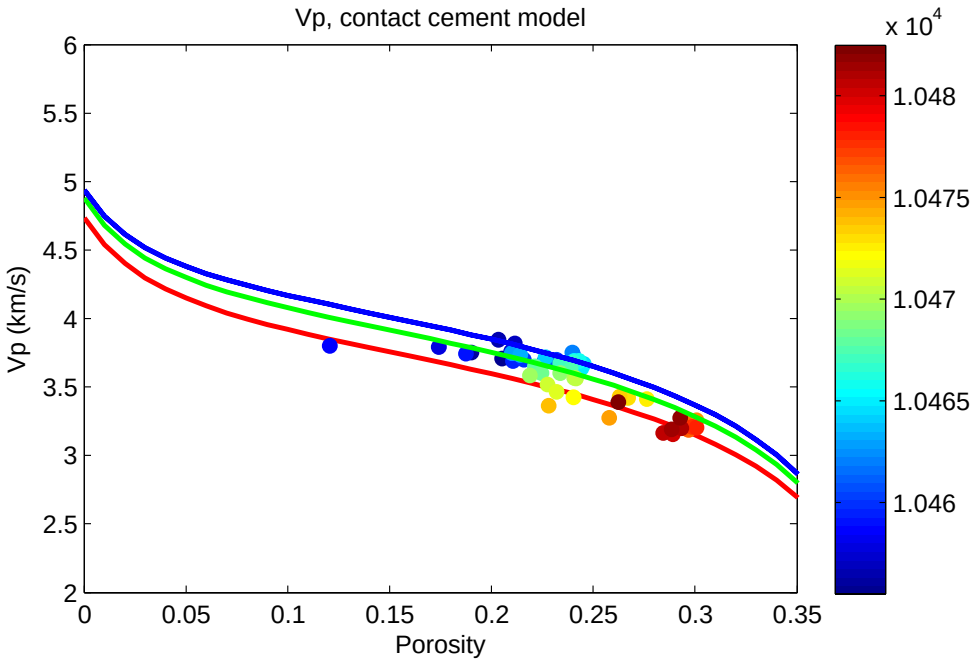

Figure 4. Vp versus total porosity (points) from the upper reservoir zone, colored by depth. Lines are from the constant cement model for different rock frame composition. The blue line represents 80% quartz, and 5% each clay, feldspar, muscovite, and calcite. The green line represents a mineral composition of 70% quartz, 10% each clay and feldspar, 7% muscovite, and 3% calcite. The red line represents 60% quartz and 20% each clay and feldspar. These different compositions bracket the data and follow the same trend as the data points although scatter is present in the data.

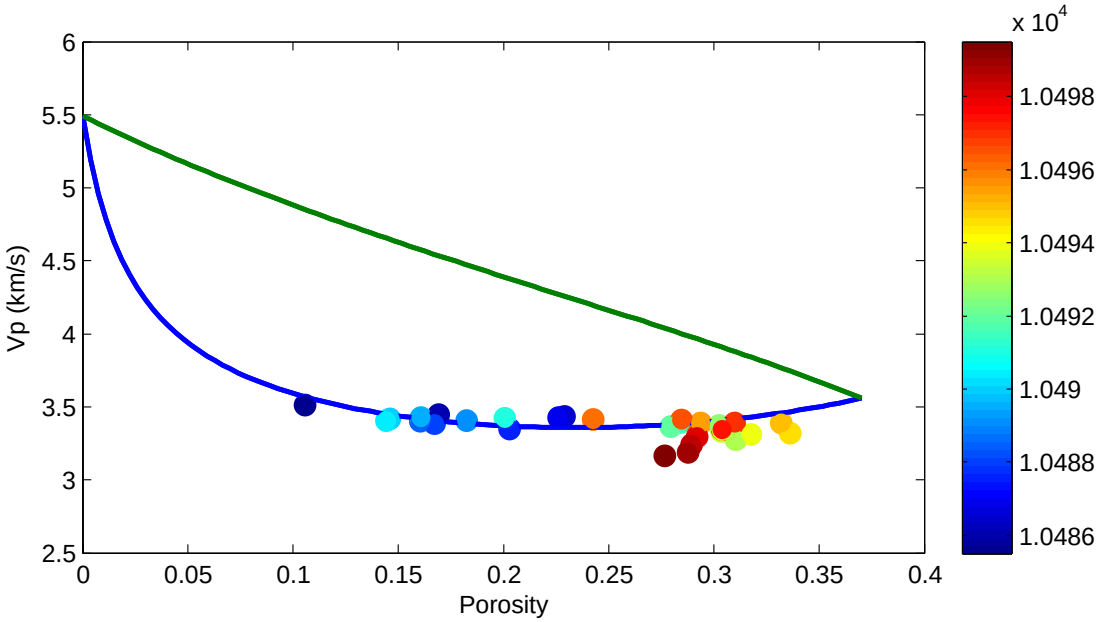

Figure 5. This figure shows the Vp to porosity colored by depth for the lower reservoir zone. A modified lower Hashin-Shtrikman bound (blue line) represents a sorting trend, and models the data points accurately. The lower bound describes a coarsening upwards sequence of the grains with better sorting at the top of the interval relative to the bottom.

Fluid Substitution and Upscaling

The first step for fluid substitution was to determine the in-situ moduli of the reservoir, rock frame, and pore fluid. Reservoir mineralogy from Hashin-Shtrikman bounding and contact theory models was estimated to be 61% quartz, 18% clay, 17% feldspar, 3% muscovite, and 1% calcite. This composition gives a mineral density of 2.678 g/cc for the reservoir interval and a mineralogical basis for calculating the required moduli. Using the calculated mineral density, the density porosity from the well log was corrected. Initial fluid saturation of the reservoir was estimated using Archie's (1942) law with m and n coefficients of 1.6 and 1.7, respectively.

The method used for fluid substitution in this study was based on the Gassmann equations (Gassmann, 1951; Biot, 1956). Equation 1 is used to calculate bulk moduli, and Equation 2 demonstrates the assumption that the shear moduli are equivalent in the saturated and dry cases.

$$\frac{K_{dry}}{K_0 - K_{sat}} = \frac{K_{dry}}{K_0 - K_{dry}} + \frac{K_{fl}}{f(K_0 - K_{fl})} \tag{1}$$

$$\frac{1}{\mu_{dry}} = \frac{1}{\mu_{sat}} \tag{2}$$

In these equations K_{dry} is the dry rock bulk modulus, K_{sat} is the saturated rock bulk modulus, K_0 is the bulk modulus of the mineral phase of the rock, and K_{fl} is the bulk modulus of the pore fluid. These equations result in accurate calculations, provided that the following criteria are met. A homogeneous mineral modulus exists; the rock is isotropic; and low frequency to maintain pore-pressure equilibrium (Gassmann, 1951).

For the fluid substitution portion of this study a rewrite of Equation 1 solved for K_{dry} (Equation 3) and K_{sat} (Equation 4) was used.

$$K_{dry} = \frac{K_{sat}(f K_0/K_{fl} + 1 - f) - K_0}{f K_0/K_{fl} + K_{sat}/K_0 - 1 - f} \tag{3}$$

$$K_{sat} = \frac{f(1/K_0 - 1/K_{fl}) + 1/K_0 - 1/K_{dry}}{(f/K_{dry})(1/K_0 - 1/K_{fl}) + (1/K_0)(1/K_0 - 1/K_{dry})} \tag{4}$$

First K_{dry} was calculated for the rock frame by using an initial K_{sat} generated from the Vp, Vs and density logs. A K_0 was determined from the mineral composition listed above, and a K_{fl} was determined by using the Sw calculated from Archies law. Then K_{dry} was used in conjunction with a range of K_{fl} values, depending on CO_2 percentage, to determine K_{sat}.

To determine the fluid substituted K_{sat} value, different K_{fl} values ranging from 100% brine to 100% CO_2 were used in the Gassmann equations. Intermediate fluid mixtures were calculated at 25, 50 and 75% CO_2 with the remaining pore fluid modeled as brine. Fluid properties are listed in Table 1. Properties for CO_2 were calculated from Span and Wagoner (1994) for an effective pressure of 30 Mpa and a temperature of approximately 100° C. These were approximate reservoir conditions during injection (Lu et al., 2012). The properties of each brine/CO_2 mixture were then calculated for each different percent CO_2 using both the Voigt (1907) bound

representing patchy saturation, and the Reuss (1929) bound, representing uniform saturation (Knight and Nolen-Hoeksema,1990).

Fluid	Density (g/cc)	Bulk Modulus (Gpa)
Brine	1.045	2.2
CO2	.675	.1275

Table1. Brine and CO_2 parameters used for fluid substitution analysis.

Both measured and fluid-substituted velocity and density logs were upscaled using the Backus (1962) average to estimate the fluid sensitivity at the seismic scale. The Backus average is the arithmetic average of the density (Equation 5) combined with the harmonic average of the elastic moduli (Equation 6). The result is the long wavelength effective medium velocity (Equation 7). This imitates low-frequency seismic data, as opposed to the high-frequency well logs. The fluid substitution curves were upscaled to 20 and 50 Hz, which were estimated to bracket the dominant frequency of surface seismic data.

$$r_{av} = \sum_k f_k r_k \tag{5}$$

$$M_{EMT} = \left(\sum_k \frac{f_k}{M_k}\right)^{-1} \tag{6}$$

$$V_{EMT} = \sqrt{\frac{M_{EMT}}{\rho_{av}}} \tag{7}$$

Amplitude Versus Angle Modeling

The next phase of work was AVA modeling. This was performed by using a half-space model. Elastic properties for the upper layer came from the shale sequence overlying the reservoir and the properties for the lower layer came from the reservoir zone. The AVA responses were calculated using the full Knott-Zoeppritz equations (Knott, 1899; Zoeppritz, 1919). These equations are used to calculate the reflection coefficients at different angles of incidence, written as a single 4x4 matrix (Equation 8).

$$\begin{pmatrix} \sin(\theta_1) & \cos(\phi_1) & -\sin(\theta_2) & \cos(\phi_2) \\ -\cos(\theta_1) & \sin(\phi_1) & -\cos(\theta_2) & -\sin(\phi_2) \\ \sin(2\theta_1) & \frac{V_{P1}}{V_{S1}}\cos(2\phi_1) & \frac{\rho_2 V_{S2}^2 V_{P1}}{\rho_1 V_{S1}^2 V_{P2}}\sin(2\theta_2) & -\frac{\rho_2 V_{S2} V_{P1}}{\rho_1 V_{S1}^2}\cos(2\phi_2) \\ -\cos(2\phi_1) & -\frac{V_{S1}}{V_{P1}}\sin(2\phi_1) & -\frac{\rho_2 V_{P2}}{\rho_1 V_{P1}}\cos(2\phi_2) & -\frac{\rho_2 V_{S2}}{\rho_1 V_{P1}}\cos(2\phi_2) \end{pmatrix} \begin{pmatrix} Rpp \\ Rps \\ Tpp \\ Tps \end{pmatrix} = \begin{pmatrix} -\sin(\theta_1) \\ -\cos(\theta_1) \\ \sin(2\theta_1) \\ -\cos(2\phi_1) \end{pmatrix} \tag{8}$$

A Monte Carlo simulation was run to estimate the range of reflection coefficients that could be expected between the overlying shale and the reservoir. A Monte Carlo technique was chosen because it returns a range of possible outcomes and allows for the probability of each outcome to be determined. This range of outcomes can be related to the variability in the rock and elastic properties. This is in contrast to calculating an AVA response from the average of the shale

layer and an average of the reservoir interval, which would only return one value. Computing just the averages does not provide for variations within each individual layer represented in the outcome. Furthermore, it does not provide a reliable representation of the interface between the two layers (Bosch et al., 2007).

Five hundered simulations were computed for each different fluid composition of 0, 25, 50, 75, and 100% CO_2. In each simulation a single depth was selected randomly from the overlying shale zone and from the reservoir zone. The velocities and densities associated with each of these depths were then used to calculate the AVA response out to 30 degrees. For each fluid composition, a bivariate PDF was calculated for the 500 simulations. Those PDFs indicate the probability of a reflection coefficient occurring at a given angle of incidence.

CLASSIFICATION

Synthetic logs calculated using fluid sbustitution were used to generate cross plots of p-impedance (Ip) to Vp/Vs, Vp, Vs, of Vp to Vp/Vs, Vs, and s-impedance (Is), and of Vs to Vp/Vs and Is. These cross plots were chosen because they represented a wide range of parameter combinations. These combinations can be extracted from well logs and from seismic and VSP data. Extracting these from seismic data is a future research topic. A bivariate PDF also was computed for each crossplot. These PDFs were used to classify the data in terms of pore fluids.

Classification success rates were calculated by mapping both the measured well log and modeled data back to the their respective bivariate PDFs. Each data point was mapped to the PDF that showed the highest probability at the location of the data point. The success rate was defined as the number of correctly classified points divided by the known number of points in that class. In initial tests, modeled data was mapped between pure brine and pure CO_2 for maximum variability in the elastic response due to fluid content. The parameter combinations that showed the highest success rates were Vp/Vs-Ip, Vp/Vs-Vp and Vp/Vs-Vs. Therefore, these combinations of elastic properties were used to examine other fluid compositions. These fluid compositions included 0 and 25, 0 and 50, and 0 and 75 % CO_2. The different CO_2 concentrations were also tested against measured well log data. When an equal probability occurred of a data point belonging to both classes, the data point was mapped to both. However, if probability in both PDFs was 0, the data point was mapped to neither class.

RESULTS

Fluid Substitution and Backus Averaging

The fluid-substitution step resulted in eight modeled Vp and Vs curves and five modeled density curves in addition to the measured data (Figure 6). Each velocity curve corresponds to the percent CO_2 that comprised the pore fluid and the bound from which the fluid moduli were calculated (Voigt or Reuss). The Vs calculated from Gassmann's equations did not change based on the method used to calculate the fluid moduli. The changes in modeled Vs as a function of CO_2 were based on density.

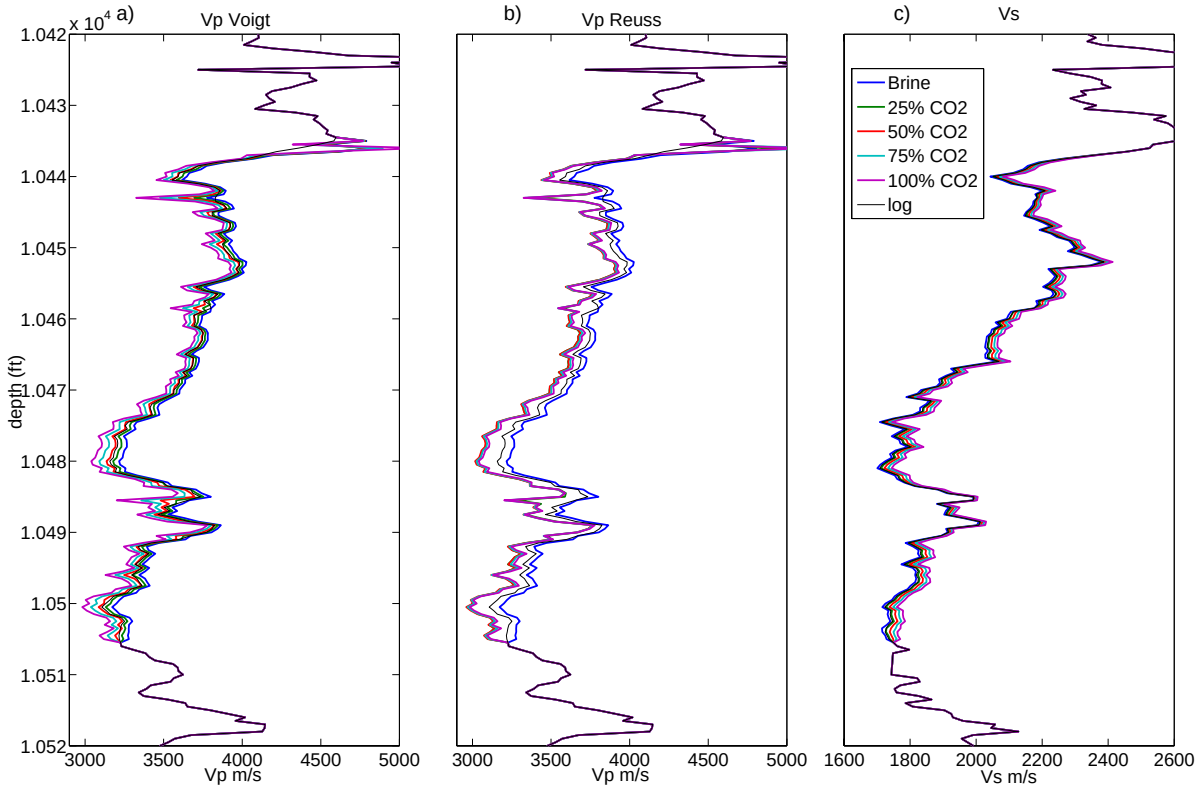

Figure 6. Panel a shows the fluid substituted velocity curves with fluid moduli calculated from the Voigt average. Panel b shows the same, but the fluid moduli were calculated with the Reuss average. Panel c shows Vs data. In these graphs the blue, green, red, cyan, and magenta lines represent pure brine, 25, 50, 75 and 100% CO_2, respectively. The thin black line on all graphs is the recorded log data, and it is included as a reference. Note that in panel a there is a uniform spacing between different fluid compositions because the Voigt average is linear. In panel b there is a large gap between the brine saturated curve and the curves containing partial or full CO_2 saturation because the Reuss average moduli change dramatically at low CO_2 concentrations and remains fairly flat with increasing CO_2. In panel c, because changes in Vs due to fluid substitution are only a function of density, Vs increases with increasing gas saturation.

End member (0 or 100% CO_2) velocity curves were independent of how the fluids were mixed, as expected. Velocity curves from the reservoir interval, with fluid moduli calculated from the Voigt bound, are shown in Figure 6a. Figure 6b shows the velocity curves for the same reservoir interval using the Reuss bound for the fluid moduli for the different fluid compositions. Figure 6c shows Vs curves for the reservoir. In all panels of Figure 6 the blue curve represents a 100% brine-saturated rock. The green, red, cyan, and magenta lines show the modeled data for 25, 50, 75 and 100% CO_2, respectively. The thin black line is the measured log data. In Figure 6a there is a uniform spacing between different fluid composition, corresponding to the linearity of the Voigt average. The Reuss average, on the other hand, shows a large decrease in velocity with a small amount of dissolved CO_2. Very little difference exists among the lines with CO_2 included. Figure 6c shows Vs increasing as CO_2 saturation increases because density decreases as a function of fluid density.

Figure 7 shows the same curves as displayed in Figure 6, up-scaled to 50Hz. It is evident in the figures that the difference in the velocity at the log scale between pure CO_2 and pure brine are larger than the differences between the corresponding velocities at the seismic scale. This is due to the long-wavelength approximation being affected by the reservoir layer and the encasing units. Wavelengths and the distance between the source and receiver are short enough, for well log measurements, that only the properties of the reservoir or the shale are measured in each sample except for samples take across the reservoir shale interface.

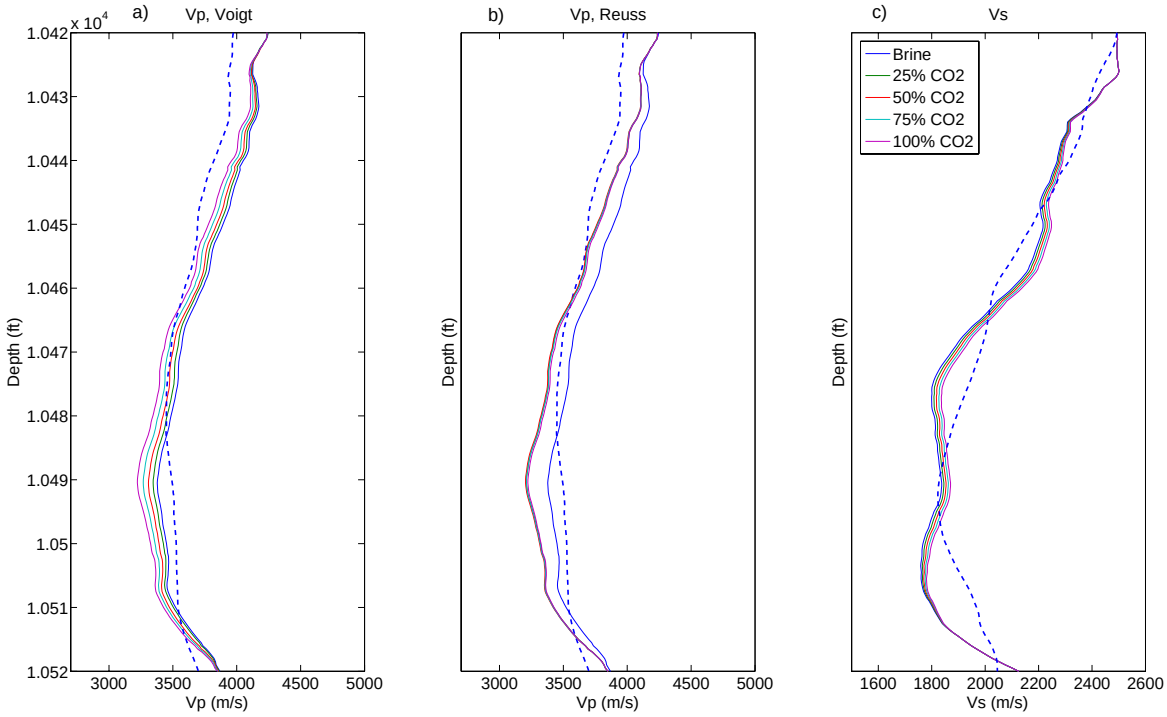

Figure 7. Panels a, b, and c show the upscaled data from Figure 6 a, b, and c, respectively. In all panels the colored lines represent different fluid compositions upscaled to 50Hz. The blue dashed line in all panels represents a pure CO_2 pore fluid upscaled to 20Hz for reference. Panel b illustrates that at seismic frequencies, differentiating between different percent CO_2 concentrations would be difficult if the fluids are mixed uniformly.

AVA

Angle-dependent reflectivity was calculated using the full Zoeppritz equations, for incidence angles of zero to thirty degrees. Five hundred Monte Carlo simulations were computed for each fluid composition (0, 25, 50, 75, and 100% CO_2). Additionally, the same number of simulations was run based on the measured log data. Figure 8 shows the AVA plots generated from the logs in Figure 6a. Panels a through e show CO_2 percentage in the fluid of 0, 25, 50, 75, and 100, respectively. Panel f shows the AVA responses generated from the measured well log data. All panels show reflection coefficients on the vertical axis and angle of incidence on the horizontal axis. Warm colors represent a high probability of generating a given reflection coefficient at a

given angle, whereas cool colors indicate a low probability. The black line represents the mean curve for each fluid scenario. The increase of reflection coefficient with increasing angle is consistent with a shale over sand sequence. In each case, high probability regions correspond to negative intercepts and less negative to zero values at 30°.

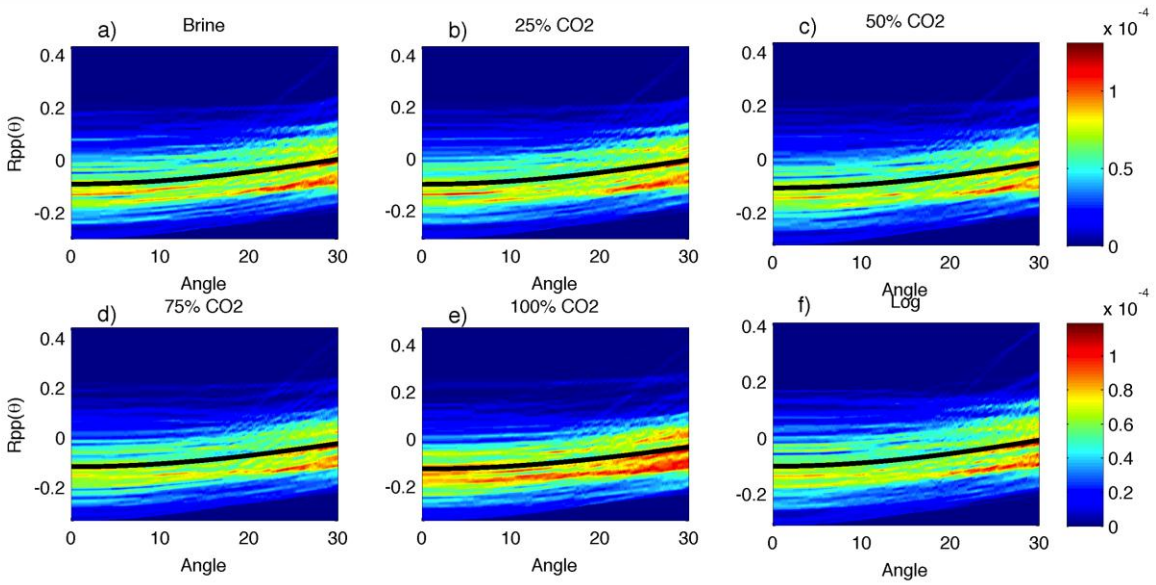

Figure 8. Each different panels shows a PDF from a Monte Carlo simulation with 500 iterations. Warm colors indicate high probability density and cool colors low probability density. Plots a-e were computed with the lines from Figure 6a. Minimal apparent difference exists between the AVA probability plots for pure brine and pure CO_2 (a and e).

Figure 9 shows the same information as Figure 8 only the curves used to generate the AVA plots were calculated using logs in Figure 6b. The results in Figure 9 are very similar to those in Figure 8 for each corresponding panel. Negative intercepts are present as are increasing values with increasing angle. Intercept (zero-angle reflection coefficient), is plotted against the AVA gradient for 100% brine (blue), 100% CO_2 (green), and measured log data (red) (Figure 10). Figure 10 illustrates that even for the CO_2 and brine end members, there is little variation between the intercept and gradient of the modeled data compared to the measure data.

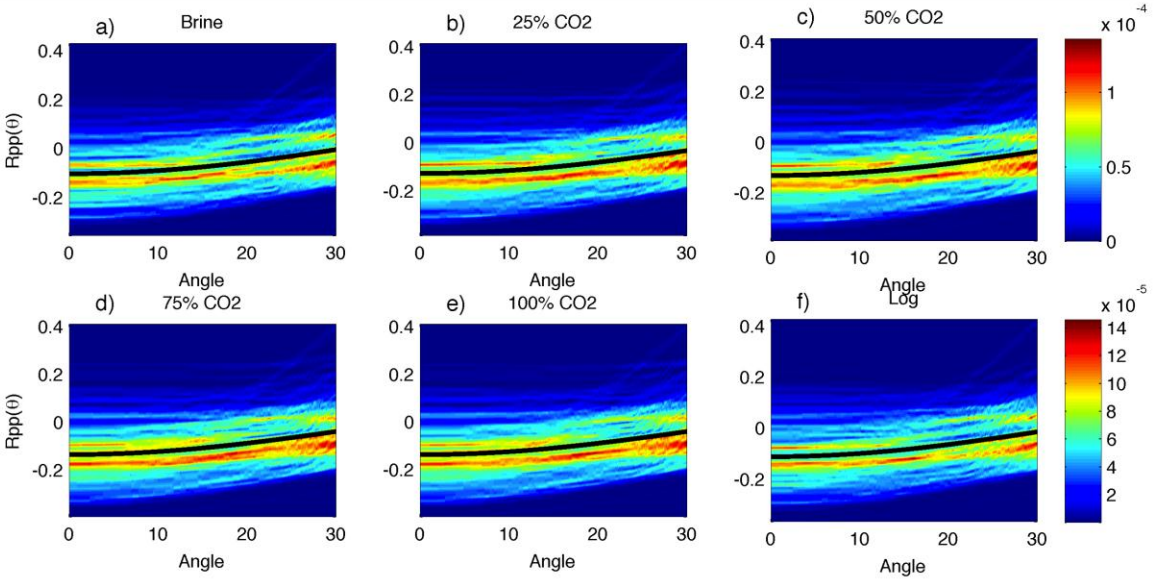

Figure 9. This is a similar plot to Figure 8. However, the logs from Figure 6b were used to compute these plots. Minimal difference betweens exist the plots for pure brine and pure CO_2 (a and e). The end members and log data look different from their corresponding plots in Figure 8. This is because the random values selected in this simulation differ from the 500 random values used for the simulation used to generate the data for Figure 8.

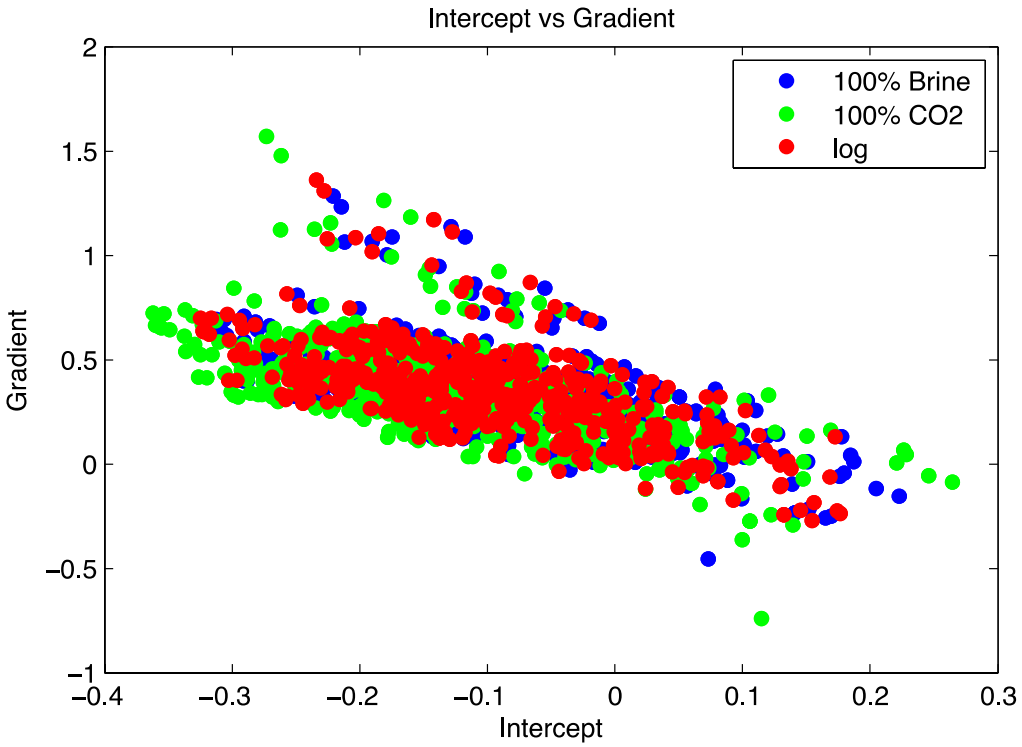

Figure 10. This AVA intercept to gradient plot further illustrates the lack of variation among the modeled AVA responses. Green points are for 100% CO_2, blue for 100% brine, and red for measured log data. In this diagram all three data sets plot almost directly atop each other with little or no statistical variation among them.

CLASSIFICATION

Modeled data from the fluid substitution step was plotted to the following cross plots: Ip to density, porosity, Vp/Vs, Vp, and Vs. Vp was plotted against Vp/Vs, Vs, and Is. And Vs was cross plotted against Vp/Vs and Is. Bivariate PDFs were generated from the data crossplots for each class, where class refers to a different fluid composition. There are six classes total. Only two classes were considered here, those for 100% CO_2 and 100% brine. Each class was mapped to its respective PDF to determine the success rate (Figure 11). Figure 11a shows 100% CO_2 (blue) and 100% brine (green) data plotted by Vp/Vs as a function of Ip. Panel b and c show the PDFs generated from the CO_2 and brine data in panel a, respectively. In panels b and c dark colors are areas of high probability, light colors are areas of low probability, and white are areas of zero probability. The success rates for each of the different cross plots tested is recorded in Table 2. The second column shows the success rate of mapping pure CO_2 to the correct PDF, and the third column shows the success rate of mapping pure brine to the correct PDF. The two fluid end members were chosen because they corresponded to the largest variations in velocity and density. The expectation was that the highest mapping success rate would occur for these two classes.

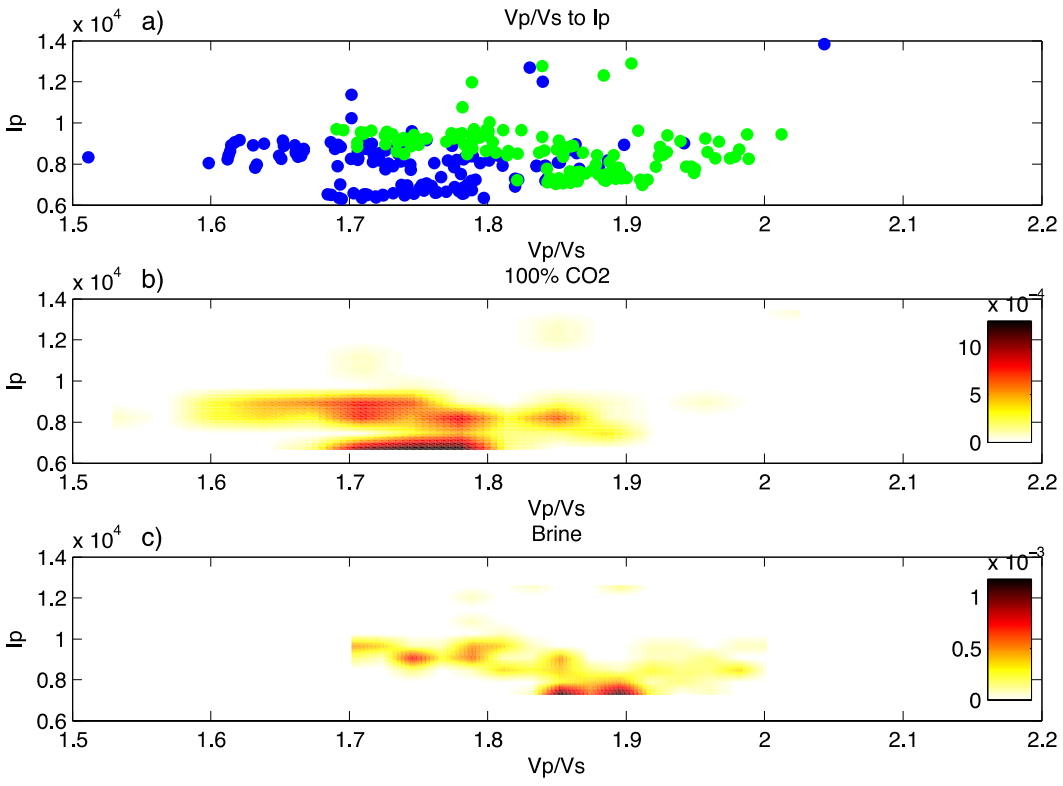

Figure 11. Panel a) Ip as a function of Vp/Vs for 100% CO_2 (blue) and 100% brine (green). b) and c) show the bivariate PDFs computed for the data in a), for the 100% CO_2 and the 100% brine data, respectively. For b) and c) black and red indicate areas of high probability density, wheras light yellow and white indicate areas of low probability or zero probability density.

Sensitivity of elastic properties to CO_2

Cross Plot	Correct map to 100% CO_2	Correct map to 100% Brine
Vp to Ip	.917	.319
Vp/Vs to Ip	.722	.620
Vs to Is	.700	.567
Vp/Vs to Vp	.695	.704
Vp/Vs to Vs	.680	.726
Vs to Ip	.617	.807
Φ to Ip	.542	.681
Vs to Vp	.500	.737
Vp to Is	.452	.674
ρ to Vp	.450	.746

Table 2. Success of mapping 100% CO_2 and 100% brine to their respective histograms. Ordered by highest to lowest correct map to CO_2. However, the same combination of elastic properties did not correspond to the highest success rates for the two fluid classes.

The three cross plots that showed the highest success rates for both fluid classes were Vp/Vs-Ip (Figure 11), Vp/Vs-Vs (Figure 12) and Vp/Vs-Vp (Figure 13). These are in rows 2,4, and 5 in Table 2, respectively. In Figure 12a Vs as a function of Vp/Vs was used to cross plot 100% CO_2 and 100% brine data, blue and green, respectively. The data in panel a was used to calculate the PDFs shown in panels b and c that correspond to 100% CO_2 and 100% brine data, respectively. Colors in figures 12a and 12b signify the range of probability from low (light) to high (dark) with white showing zero probability. The axes in Figure 13 show Vp as a function of Vp/Vs. Data plotted in Figure 13a corresponds to 100% CO_2 (blue) and 100% brine (green). The 100% CO_2 data was used to generate the PDF shown in Figure 13b and the 100% brine data was used to generate the PDF shown in Figure 13c. Figures 13a and b are colored to the same scheme as their counterparts in Figures 11 and 12.

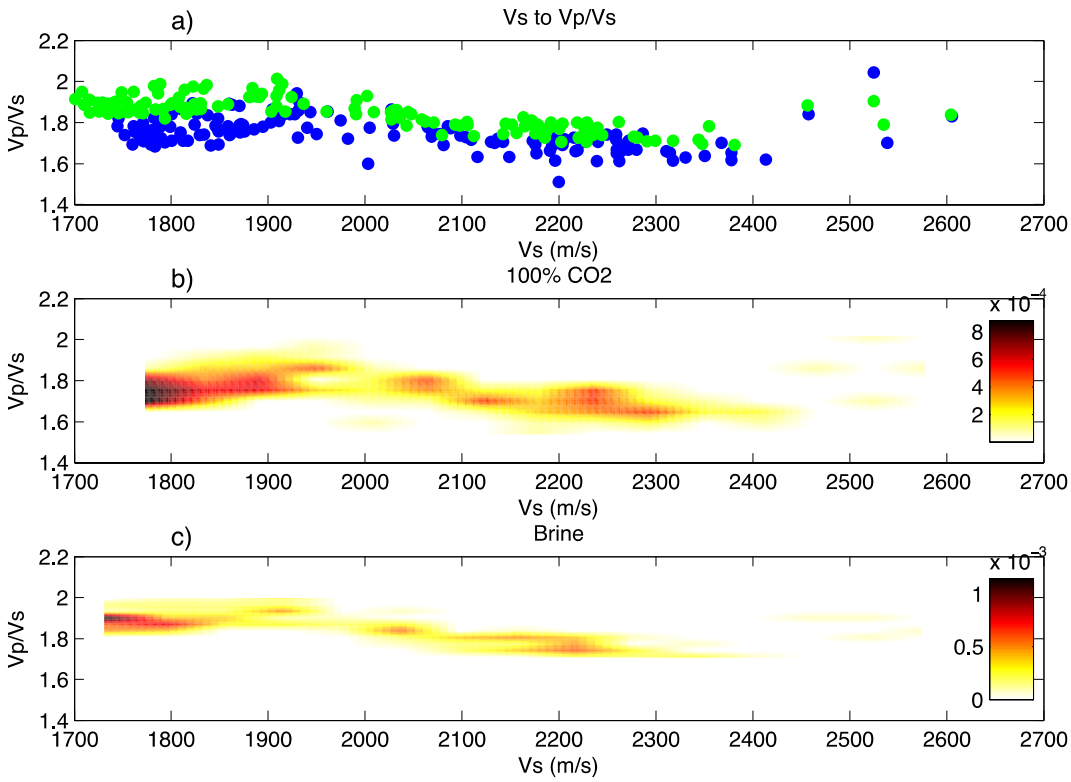

Figure 12. a) shows modeled data for 100% CO_2 (blue) and 100% brine (green) for Vs as a function of Vp/Vs. b) shows the bivariate PDF generated from the 100% CO_2 data points, and c) shows the bivariate PDF generated from the 100% brine data. Color in b) and c) range from black and red (high probability density) to light yellow and white (low or zero probability density).

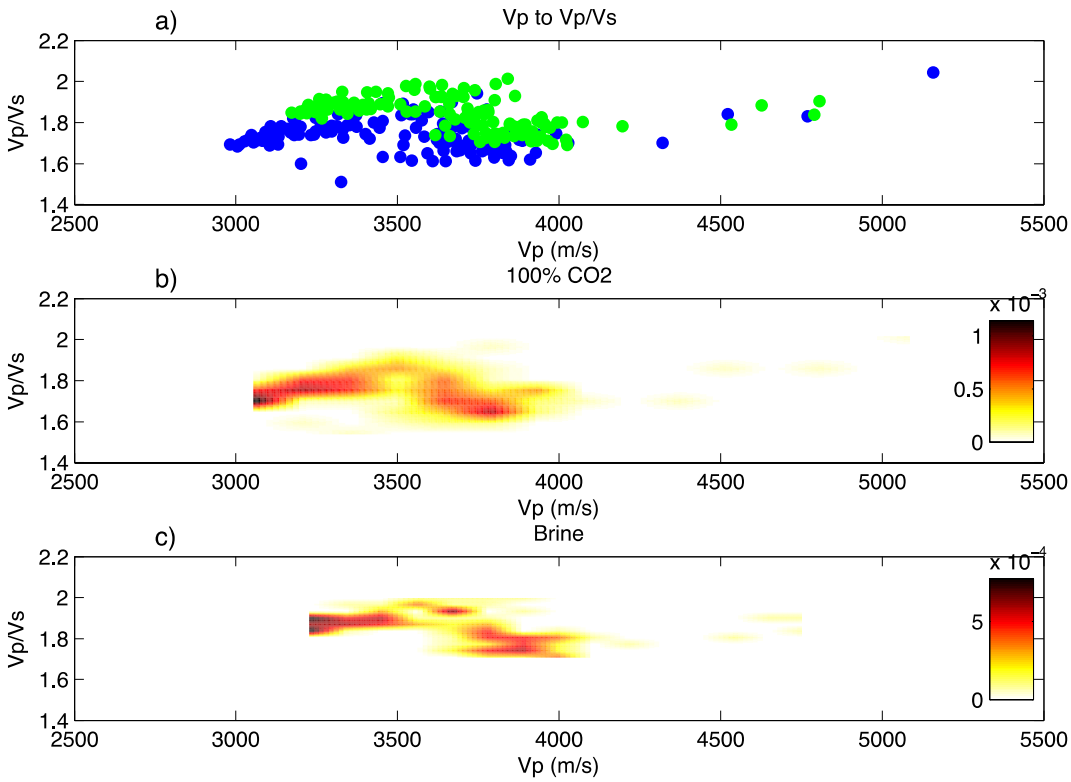

Figure 13. This figure is Vp as a function of Vp/Vs. a) shows blue and green data representing 100% CO_2 and 100% brine, respectively. b) and c) show the bivariate PDFs generated from the 100% CO_2 and 100% brine data from panel a. Black and red colors indicate high probability density. Light yellow and white indicate low probability density.

Results from classifying the intermediate fluid compositions generated lower success rates than did classifying of the end members, as expected. Table 3 shows the results of mapping intermediate fluid compositions against brine and against measured log data. In Table 3 the six columns of data represent the results of plotting 25, 50 and 75 % CO_2 concentrations against measured data (columns 2 through 4) and against 100% brine (columns 5 through 7). Fluid moduli were calculated as a lower bound in Table 3.

Cross Plot	25/log	50/log	75/log	25/0	50/0	75/0
Vp/Vs to Ip	.478/.732	.617/.683	.664/.577	.593/.688	.693/.602	.735/.495
Vp/Vs to Vs	.550/.835	.628/.727	.627/.672	.519/.857	.675/.761	.698/.597
Vp/Vs to Vp	.576/.815	.641/.704	.638/.652	.671/.713	.705/.692	.733/.645

Table 3. The intermediate fluid concentrations mapped to their respective PDFs for the three best performing cross plots from Table 2. Fluid properties were calculated from the Reuss average.

Table 4 shows the same data as Table 3 except that the fluid parameters were calculated with the upper bound. The results showed that there was, in general, an increase in the success rate with an increase in percent CO_2 for both methods of generating fluid moduli. When using the Reuss, average only slight increases occurred in success rates with increases in CO_2 percentage.

However, success rates of data derived from the Voigt bounds displayed a larger increase in success rate with increasing % CO_2 compared to the respective class calculated with the Reuss bound. The highest success rate for either fluid modeling method occurred for Vp against Vp/Vs ratio, with Vs against Vp/Vs showing a similar but slightly reduced success rate as compared to plotting Vp to Vp/Vs.

Cross Plot	25/log	50/log	75/log	25/0	50/0	75/0
Vp/Vs to Ip	.322/.577	.440/.642	.522/.672	.505/.447	.621/.514	.636/.611
Vs to Vp/Vs	.459/.537	.458/.606	.492/.811	.385/.692	.631/.878	.549/.833
Vp to Vp/Vs	.385/.611	.445/.630	.496/.748	.491/.487	.626/.624	.646/.684

Table 4. The intermediate fluid concentrations mapped to their respective histograms for the three best performing cross plots from Table 2. Fluid properties were calculated from the Voigt average.

DISCUSSION

Fluid composition and the mixing of fluid moduli play an important role in the velocity modeling. If the fluids are mixed using a patchy saturation model, there is a linear trend in Vp with changes in CO_2 saturation. When the fluids are mixed uniformly, as is represented by the Reuss bound, it is evident (Figure 6b) that little variation in velocity exists among concentrations of CO_2 of 25 to 100 %. However, there is a substantial change in velocity between 100% brine and 25 % CO_2. This supports previous work that indicates that velocities are dependent on fluid saturations and on the way those fluids are distributed within the pore space (Mavko and Mukerji, 1998). This phenomenon is similar to the commonly recognized fizz-water problem, where a small amount of gas corresponds to a large decrease in velocity, but additional increases in gas saturation minimally decrease velocity. The consistency between the modeled Vs values is easily understood because only density affects Vs (Figure 6c). Bulk density changes linearly with changes in CO_2 percent because it is calculated from a weighted average of fluid components and rock frame minerals.

The upscaled log data, as expected, shows a smoothed version of the high-frequency log data. Wavelength is a function of frequency and velocity. Because Vs is less than Vp in a given medium, the smoothing affects of upscaling Vs data will not be as pronounced for a given frequency as those for Vp data. This indicates that Vs data has the potential to provide a higher resolution data set at low frequencies than does Vp data.

A lack of variation in the AVA modeling is evident in the results. All panels of Figure 8 and Figure 9 show very similar reflection coefficients at all angles regardless of fluid composition or fluid mixing. Additionally, there is a clear lack of discrimination among the data sets presented in Figure 10. The three different fluid classes plot nearly atop one another with little if any discrimination amongst them.

The lack of variation in the AVA response can be explained by realizing that the stiff rock frame of the sand, due to the cement, is independent of any AVA effects. The stiff frame restricts the sensitivity of the rock elastic properties to fluid changes (Castagna and Backus, 1993). Given the stiffness and high velocities associated with the reservoir material in this study, it is expected that there will be only a small amount of variation in the AVA response with a

change in fluid composition. Additionally, the larger the contrast in the rock properties across an interface, the smaller the affect the fluid will have on the reflection coefficient (Stine, 2004). Due to the internal stiffness of the sand, neither the Ip nor the Is of the reservoir change significantly with changes in fluid composition. AVA affects are a function of Ip and Is across the reservoir/shale interface. At zero angle the large contrast in Ip gives a reflection coefficient with a large magnitude (negative intercepts in Figures 8 and 9). However, as the angle of incidence increased, the reflection coefficient becomes primarily a function of Is and density. Because Is and density do not change significantly with a change in fluid content, it is difficult to attribute changes in AVA effects to fluid variations.

Results from the classification scheme showed a relatively high success rate when using combinations of Vp/Vs-Vp, Vp/Vs-Vs and Vp/Vs-Ip. Each combination contains Vp/Vs. These occurrences indicate that Vp/Vs can be important and useful for characterizing and monitoring injected CO_2. With the method used in this study, if the probability was zero in both classes, data was not mapped to either class. However, due to the coarse bin spacing that was used in this study, areas where the density of data was relatively low had the potential to indicate a probability density of zero. Additionally these results show that the larger the difference in elastic parameters among the pore fluid the higher the detection rate will be.

When examining the scatter plots of the data and the bivariate PDFs, sharp edges are present along the boundaries of the PDFs between a high probability and zero probability. This is an artifact of the binning when computing the PDFs. It has the potential to have a small negative impact on successfully mapping data sets back to their respective classes. Figure 14a shows the PDF for 100% CO_2 pore fluid, and Figure 14b shows the PDF for 100% brine pore fluid. Black points in both panels are the data corresponding to the PDFs. Because of the binning procedure, some data points fall off the edge of their respective PDFs. During the mapping routine, these data points were not mapped to either histogram. One way to minimize this affect in future studies would be to simulate statistically equivalent data points to increase the total number of data points used to compute the PDF. This could help to extend the range of the PDF and smooth the edges to avoid the juxtaposition of high and low probability density regions.

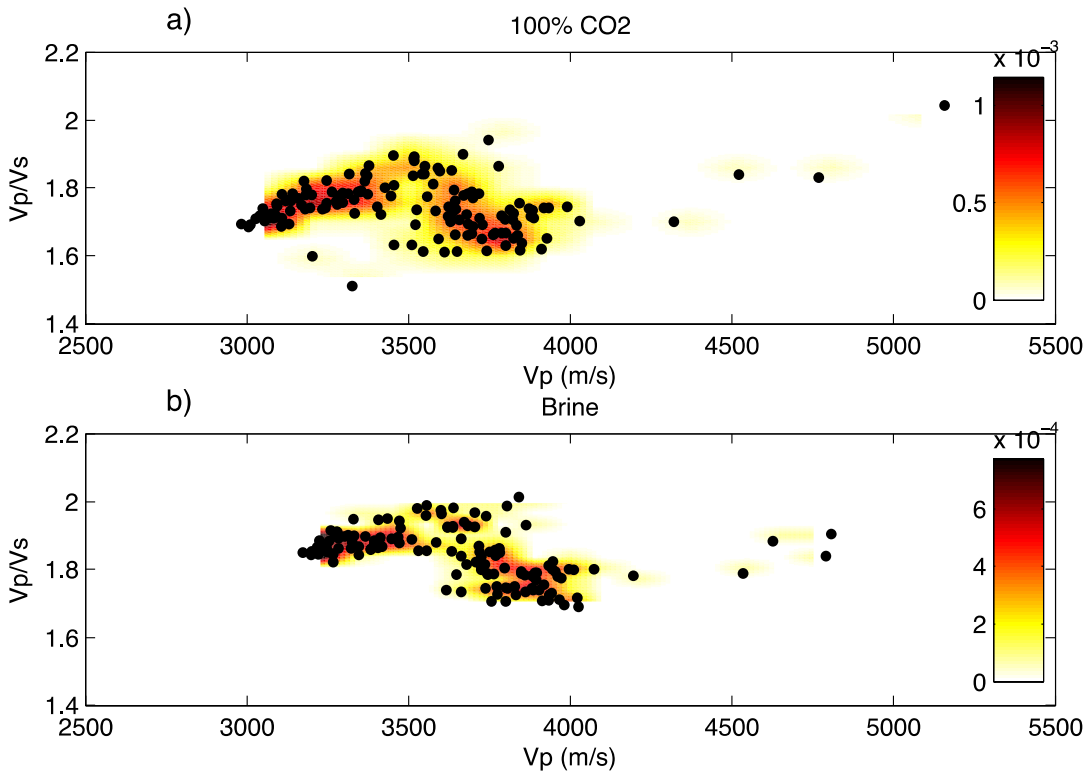

Figure 14. Modeled data plotted atop its correspondng bivariate PDF. Panel a shows 100% CO_2 data and panel b shows 100% brine data. Red and black colors in these panels represent high probability density, whereas light yellow and white represent low probability density. These plots illustrate that there are some are, especially at the left of the PDFs, where a relatively high density of data points plot into a zero probability region.

When using Vs in the classification of the data for 0 and 50% CO_2, a lower success rate occurs relative to mapping 0 and 25% CO_2. This is counter-intuitive because convention indicates that the more dissimilar the fluid composition is, the higher the ability to correctly map the data. This anomaly can be explained by looking at the movement of the histograms when increasing CO_2 from 25 to 50 % as can be seen in Figure 15. In Figure 15 the blue contour plot is 50 % CO_2, the red contour plot is 25 % CO_2 and the green contour plot is 100% brine. When fluid properties are calculated by the Voigt average, as in Figure 15, change in Vp is negative whereas the change in Vs is positive for a given change in fluid composition. Because of this, the histograms in this situation shift laterally along the x-axis showing predominantly a change in Vs only. This causes the highest probability region of the 50% CO_2 class (blue) to overlie the 100% brine (green) class such that mapping to the 25% CO_2 class (red) is negatively affected. This could also be mitigated by statistically extending the data sets.

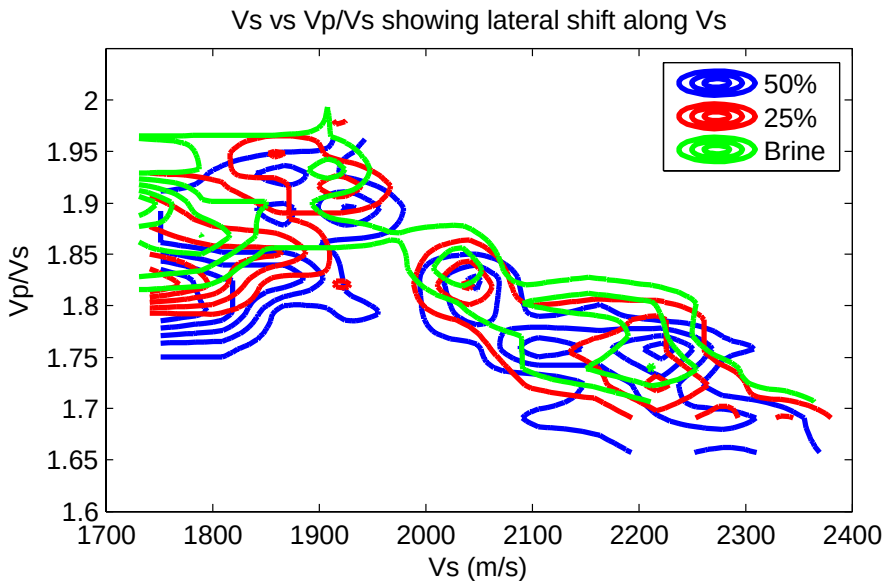

Figure 15. Probability contours for 50, 25% CO_2, and 100% brine saturations in blue, red and green, respectively. This illustrates the lateral shift in Vs that can happen with even a small change in fluid properties when the fluid moduli are calculated using the Voigt bound. The result is a lower classification success rate for intermediate CO_2 concentrations.

CONCLUSIONS

This study showed that AVA may not be reliable when examining fluid substitution in a reservoir that is very stiff or when there is a strong contrast in impedance across an interface. When looking at a shale-sandstone interface with a large impedance contrast, the reflection coefficient will not show significant changes with respect to changes in fluid composition. Because the changes in fluid composition do not significantly alter either the shear impedance or the density of the rock, the angle-dependent reflection coefficients will not show much variability with changes in fluid. The combination of these two factors work to minimize the change in AVA due to a change in fluid composition.

This study indicates that the way fluids are mixed can have a significant impact on the fluid properties and the overall rock properties. When mixing a liquid and a gas using the Reuss bound versus the Voigt bound, the change in moduli with respect to gas saturation is less apparent with higher gas concentrations than it is with lower gas concentrations. However, because fluid has no affect on shear moduli, when looking at the calculated Vs for a fluid-saturated rock, there is no change in the velocity regardless of which method is used to calculate the fluid parameters. Accordingly cross plots of Vp as a function of Vp/Vs and Vs as a function of Vp/Vs provide the best ability to discriminate between variations in fluid composition in a stiff rock frame. This is because Vp/Vs is density independent. According to Gassmanns equations the shear modulus of the rock is independent of the fluid. Therefore Vp/Vs also minimizes the influence of shear modulus. Because of this, changes in Vp/Vs from one pore fluid to another result from changes in the bulk modulus of the saturated rock. Although Vp/Vs cannot be used as a direct indicator of fluid composition, cross plots generated with it are useful

for comparing modeled fluid substitution data to measured data. From these crossplots, PDFs can be generated to assess the change and the uncertainty in that change for time-lapse studies.

REFERENCES:

Archie, G.E., 1942. The elextrical resistivity log as an aid in determining some reservoir characteristics. Transactions of the American Institute of Mining, Metallurgical and Petroleum Engineers, **146**, 54-62

Artola, F., Alvarado, V., 2006, Sensitivity analysis of Gassmanss's fluid substitution equations: Some implications in feasibility studies of time-lapse seismic reservoir monitoring, Journal of Applied Geophysics, **59**, 47-52.

Avseth, P., Mukerjo, T., Mavko, G., 2010. Quantitative Seismic Interpetation, New York: Cambridge University Press.

Avseth, P., Skeji, Norunn., 2011, Rock physics modeling of static and dynamic reservoir properties – a heuristic approach for cemented sandstone reservoirs, The Leading Edge, **30**, 90-96.

Backus, G.E., 1962, Long-Wave elastic anisotropy produced by horizontal layering, Journal of Geophysical Research., **68**, 4427-4440.

Biot, M.A., 1956, Theory of propagation of elastic wavers ina fluid saturated porous solid. I. Low-frequency range, Journal of the Acoustical Society of America, **28**, 168-178.

Bosch M., Cara, L., Rodrigues, J., Navarro, A., Diaz, M., 2007, A Monte Carlo approach to the joint estimation of reservoir and elastic parameters from seismic amplitudes, Geophysics, **72**, O29-O39.

Bosch, M., Carvajal, C., Rodrigues, J., Torres, A., Aldana, M., Sierra, J., 2009, Petrophysical seismic inversion conditioned to well-log data: Methods and application to a gas reservoir, Geophysics, **74**, O1-O15.

Castagna, J P. and Backus, M., 1993, Offset Dependent Reflectivity—Theory and Practice of AVO Analysis, Society of Exploration Geophysics.

Castagna, J. P., and Swan, H.W., and Foster,D. J., 1998, Framework for AVO gradient and intercept interpretation, Geophysics, **63**, 948–956.

Chadwick, A., Williams, G., Delepine, N., Clochard, V., Labat, K., Sturton, S., Buddensiek, M., Dillen, M., Nickel, M., Lima, A., Arts, R., Neele, F., and Rossi, G., 2010, Quantitative analysis of time-lapse seismic monitoring data at the Sleipner CO2 storage operation, The Leading Edge, **29**, 170-177.

Cheng, A., Huang, L., and Rutledge, J., 2010, Time-Lapse VSP data processing for monitoring CO_2 injection, The Leading Edge, **29**, 196-199.

Das, A., and Batzle, M., 2008, Modeling studies of heavy oil-in between solid and fluid properties, The Leading Edge, **27**, 1116-1123.

Dvorkin, J., Mavko, G., and Nur, A., 1991, The effects of cementation on the elastic properties of granular material, Mechanics of Materials, **12**, 207-217.

Dvorkin, J., Nur, A., and Yin, H., 1994, Effective properties of cemented granular material, Mechanics of Materials, **18**, 351-366.

Dvorkin, J. and Nur A., 1996, Elasticity of High-porosity sandstones: Theory for two North Sea datasets, Geophysics, **61**, 1363-1370.

Gassmann, F., 1951, Uber die elastizitat poroser medien, Vier. Natur Gesellschaft, **96**, 1-23.

Ghaderi, A., and Landro, M., 2009, Estimation of thickness and velocity changes of injected carbon dioxide layers from prestack time-lapse seismic data, Geophysics, **74**, O17-O28

Hashin, Z., and Shtikman, S., 1963, A Variational approach to the elastic behavior of multiphase materials, Journal of the Mechanics and Physics of Solids, **11**, 127-140

Knight, R., and Nolen-Hoeksema, R., 1990, A laboratory study of dependence of elastic wave velocities on pore scale fluid distributions, Geophysical Research Letters, **17**, 1529-1532.

Knott, C. G., 1899. Reflection and refraction of elastic waves, with seismological applications. Philosophical Magazine., London, **48**, 567-569.

Kordi, M., Hovorka, S., Milliken, K., Treviño, R., and Lu, J., 2010, Diagenesis and reservoir heterogeneity in the Lower Tuscaloosa Formation at Cranfield Field, Mississippi: presented at the 60th Annual Convention of the Gulf Coast Association of 96 Geological Societies and the Gulf Coast Section of SEPM, San Antonio, Texas, October 10-12, 2010. GCCC Digital Publication Series #10-13.

Lu, J., Kharaka, Y., Thordsen, J., Horita, J., Karamalidis, A., Griffith, C., Hakala, A., Ambats, G., Cole, D., Phelps, Manning, M., T., Cook, P., and Hovorka, S., 2012, CO_2–rock–brine interactions in Lower Tuscaloosa Formation at Cranfield CO_2 sequestration site, Mississippi, U.S.A., Chemical Geology, **291**, 269-277.

Lumley, D., 2010, 4D seismic monitoring of CO_2 sequestration, The Leading Edge, **29**, 150-155.

Mavko, G., Mukerji, T., 1998. Bounds on low-frequency seismic velocities in partially saturated rocks. Geophysics. **63**, 918– 924.

Morency, C., Lou, Y., Tromp, J., 2011, Acoustic, elastic and poroelastic simulations of CO2 sequestration crosswell monitoring based on spectra-element and adjoint methods, Geophysical Journal International, **185**, 955-966.

Mukerji, T., Jorstad, A., Avseth, P., Mavko, G., Granil, J. R., 2001, Mapping lithofacies and pore-fluid probabilities in a North Sea reservoir: Seismic inversion and statistical rock physics, Geophysics, **66**, P988-P1001.

Reuss, A., 1929. Berechnung der Fleissgrenzen von Mischkristallen auf Grund der Plastizitatsbedingung fur Einkristalle, Zeitschrift fur Angewandte Mathematik aus Mechanik, **9**, 49-58.

Russell, B. H., Heldin, K., Hilterman, F. J., Lawrence, R. L., 2003, Tutorial: Fluid-property discrimination with AVO: A Biot-Gassmann perspective, Geophysics, **68**, P29-P39.

Rutherford, S. R., and Williams, R., H., 1989, Amplitude-versus-offset variations in gas sands. Geophysics, **54**, 680-688.

Simm, R., White, R., Uden, R., 2000, The anatomy of AVO crossplots, The Leading Edge, **19**,150-155.

Span, R., and Wagoner, W., 2004, A new equation of state for carbon dioxide covering the fluid region from the triple-point temperature to 1100 K at Pressures up to 800 MPa. Journal of Physical Chemical Reference Data, **25**, No. 6, 1509-1596.

Stine, J.A., 2004, Sensitivity of AVO reflectivity to fluid properties in porous media. Unpublished Masters Thesis, The University of Texas at Ausin.

Voigt, W., 1907. Bestimmung der Elastizitatskonstanten von Eisenglanz. Anallen der Physik, **24**, 129-140.

Zoeppritz, K., 1919, ErdbebenwellenVIIIB, Ueber Reflection and Durchgang seismischer Wellen durch Unitestigkeitsflaechen. Goettinger Nachrichten, I, 66-84.